Native Two-Qubit Gates in Fixed-Coupling, Fixed-Frequency Transmons Beyond Cross-Resonance Interaction

Ken Xuan Wei,* Isaac Lauer, Emily Pritchett, William Shanks, David C. McKay, and Ali Javadi-Abhari†

IBM Quantum, IBM T.J. Watson Research Center, Yorktown Heights, New York 10598, USA

(Received 2 December 2023; revised 19 April 2024; accepted 25 April 2024; published 20 May 2024)

Fixed-frequency superconducting qubits demonstrate remarkable success as platforms for stable and scalable quantum computing. Cross-resonance gates have been the workhorse of fixed-coupling, fixed-frequency superconducting processors, leveraging the entanglement generated by driving one qubit resonantly with a neighbor's frequency to achieve high-fidelity, universal controlled-NOT (CNOT) gates. Here, we use on-resonant and off-resonant microwave drives to go beyond cross-resonance, realizing natively interesting two-qubit gates that are not equivalent to CNOT gates. In particular, we implement and benchmark native *i*SWAP, SWAP, $\sqrt{i\text{SWAP}}$, and *b*SWAP gates; in fact, any SU(4) unitary can be achieved using these techniques. Furthermore, we apply these techniques for an efficient construction of the *B* gate: a perfect entangler from which any two-qubit gate can be reached in only two applications. We show that these native two-qubit gates are better than their counterparts compiled from cross-resonance gates. We elucidate the resonance conditions required to drive each two-qubit gate and provide a novel frame tracking technique to implement them in Qiskit.

DOI: 10.1103/PRXQuantum.5.020338

I. INTRODUCTION

Fixed-frequency transmons with fixed couplings have performed quantum simulations with great success using cross-resonance (CR) gates [1], whose fidelities have increased steadily over time [2–5]. Recently, fixed-coupling transmons have demonstrated native *ZZ* interactions using off-resonant Stark tones [6,7]. It is natural to ask: can more interesting two-qubit interactions be realized natively in fixed-coupling transmons? In this manuscript we show how to generate native *i*SWAP, SWAP, *b*SWAP, and non-Clifford gates such as $\sqrt{i\text{SWAP}}$ and *B* gates using only microwave drives in a fixed-frequency, fixed-coupling transmon processor. To our knowledge, this is the first experimental demonstration of the *B* gate, introduced in Ref. [8], from which any two-qubit unitary can be compiled with only two applications. These native two-qubit gates are faster and higher fidelity than their counterparts compiled using controlled-*Z* (CZ) gates based on the CR interaction. They can be driven in any coupled two-level systems, and do not require higher levels such as the MAP gate [9]. Native two-qubit gates beyond CR can reduce circuit depth for quantum chemistry applications [10] and improve quantum volume [11] in fixed-coupling superconducting processors.

The key challenge in realizing these native two-qubit gates is that the interaction takes place in a frame that is not resonant with either qubit, and thus the phases of these two-qubit gates change depending on where they are applied in a quantum circuit. This is drastically different from CR interactions, where the CR tone is applied on the control qubit on resonant with the target qubit, and thus the CR interaction evolves in the same frame as the target qubit. Analogously, frame tracking was required in Ref. [12] to discover errors in frames that are different than the microwave drive. Here we develop and implement this functionality in Qiskit [13] by introducing a novel frame tracking technique to correctly compile the time-dependent phases associated with each two-qubit gate in the quantum circuit. We benchmark these native two-qubit gates using interleaved randomized benchmarking (IRB) [14,15]. Our manuscript is organized as follows. In Sec. II we give an overview of the frame tracking required for implementing phase sensitive two-qubit gates. In Sec. III we implement and benchmark a high-fidelity *i*SWAP gate by driving one qubit resonantly; combining this with CR allows us to implement a high-fidelity direct SWAP gate. In Sec. IV we show how native *i*SWAP and *b*SWAP gates can be implement by driving one qubit off resonantly. In Sec. V we

*Corresponding author: xkwei@ibm.com
†Corresponding author: ali.javadi@ibm.com

Published by the American Physical Society under the terms of the Creative Commons Attribution 4.0 International license. Further distribution of this work must maintain attribution to the author(s) and the published article's title, journal citation, and DOI.

implement and benchmark native $\sqrt{i\text{SWAP}}$ and B gates. This work, along with CR and native ZZ interactions, completes all possible native two-qubit interactions for fixed-frequency, fixed-coupling transmons.

II. FRAME TRACKING

In fixed-frequency, fixed-coupling superconducting processors, single-qubit and controlled-NOT (CNOT) gates using the CR interaction are implemented in the rotating frame on resonant with qubit's frequency. Consider two coupled transmons where one qubit is driven either on resonantly or off resonantly. The resulting two-qubit unitary U_g is generated by a time-independent Hamiltonian in a frame that is rotating at a different frequency from the driven qubit's resonant frequency by an offset Δ. The unitary implemented in the qubit's frame is given by

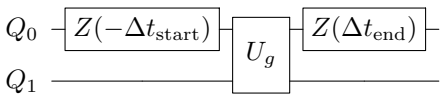

(1)

where Q_0 and Q_1 are the driven and idle qubits, respectively, $Z(\theta)$ represents rotation around z by angle θ, and t_{start} and t_{end} are the start and end times of U_g. Here we see that U_g is sandwiched between two time-dependent Z rotations, thus depending on where U_g appears in a quantum circuit, different Z rotations are needed to correct for $Z(-\Delta t_{\text{start}})$ and $Z(\Delta t_{\text{end}})$. We refer to adding time-dependent Z rotations to U_g as frame tracking. The situation is simplified for the CR gate, where Q_0 is driven at the resonant frequency of Q_1. The effective interactions are ZX and ZI, both commuting with $Z(\theta)$ on the control qubit. We can move $Z(-\Delta t_{\text{start}})$ across U_g as

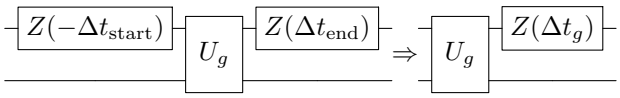

where $t_g = t_{\text{end}} - t_{\text{start}}$ is the gate time of U_g. Thus, for two-qubit gates using the CR interaction, we only need to apply a time-independent Z rotation at the end, and no frame tracking is needed. We remark that, for strongly driven CR gates, there are non-Markovian gate errors that prevent $Z(\theta)$ from fully commuting with U_g, but these errors can be removed with the derivative removal via adiabatic gate (DRAG) pulse [12,18,19].

For iSWAP gates, the phases in front of the gate can be moved to the back according to the rule

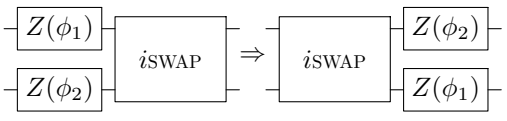

(2)

This makes iSWAP gates compatible with virtual Z rotations [20]. The frame tracking for the iSWAP gate will be discussed in detail in Sec. III. For non-Clifford gates such as the $\sqrt{i\text{SWAP}}$ gate, it is no longer possible to move Z rotations across the gate. The frame tracking can be done using physical Z rotations, and any single-qubit unitary can be implemented as three single-qubit gates [21]. We note that frame tracking has been implemented in tunable architectures such as two fixed-frequency qubits coupled via a tunable qubit [22–24], as well as a fixed-frequency qubit coupled to a tunable qubit [25].

III. ON-RESONANT DIRECT iSWAP GATE

A direct implementation of the iSWAP gate using on-resonant drives has been proposed before in Ref. [26]; to the best of our knowledge, these gates have not been experimentally implemented and benchmarked. The mechanism, called fixed linear couplings between fixed off-resonant qubits (FLICFORQ), is based on driving two coupled qubits resonantly satisfying the resonance condition $\Omega_{R1} + \Omega_{R2} = |\Delta_{12}|$, where Ω_{R1} and Ω_{R2} are the Rabi amplitudes of the resonant drives and Δ_{12} is the frequency difference between the qubits. We implement a similar approach to FLICFORQ, but we drive only on one qubit resonantly. This has two advantages: first we observe that the iSWAP rate for one-qubit driving is nearly twice the rate for dual qubit driving (FLICFORQ). In addition, it frees up the other qubit, which we can drive separately to achieve a native SWAP gate as well. The pulse sequences and iSWAP dynamics are presented in Fig. 1; the oscillations at the resonance points and the rates are provided in Appendix A.

The starting point of our analysis is the Hamiltonian of an on-resonant drive along the x axis; after the rotating-wave approximation the effective Hamiltonian is given by [12,27]

$$H_D = \frac{\Omega}{2}(XI + \mu ZX) - \frac{\Delta}{2}IZ,$$

where Ω is the Rabi amplitude of the drive, Δ is the frequency difference between the driven and idle qubit, and $\mu = J/\Delta$ with $J \approx 2$ MHz the coupling rate between the two qubits. The Rabi amplitude of the drive Ω is always taken as positive, and for simplicity, we have ignored small cross-talk terms IX and ZZ. Typically, for single-qubit gates, we operate in the regime $\Omega \ll |\Delta|$, where spectator error arising from the CR (ZX) term is small and can be neglected. As we increase the driving amplitude, significant spectator error can be observed [12]. For $\Omega = |\Delta|$, the spectator error becomes the dominant interaction and it can be used to drive an iSWAP gate. To construct the iSWAP gate, we sandwich H_D between single-qubit rotations $Y_{\pm\pi/2}$ on the driven qubit and calibrate Ω and the gate time t_g. The

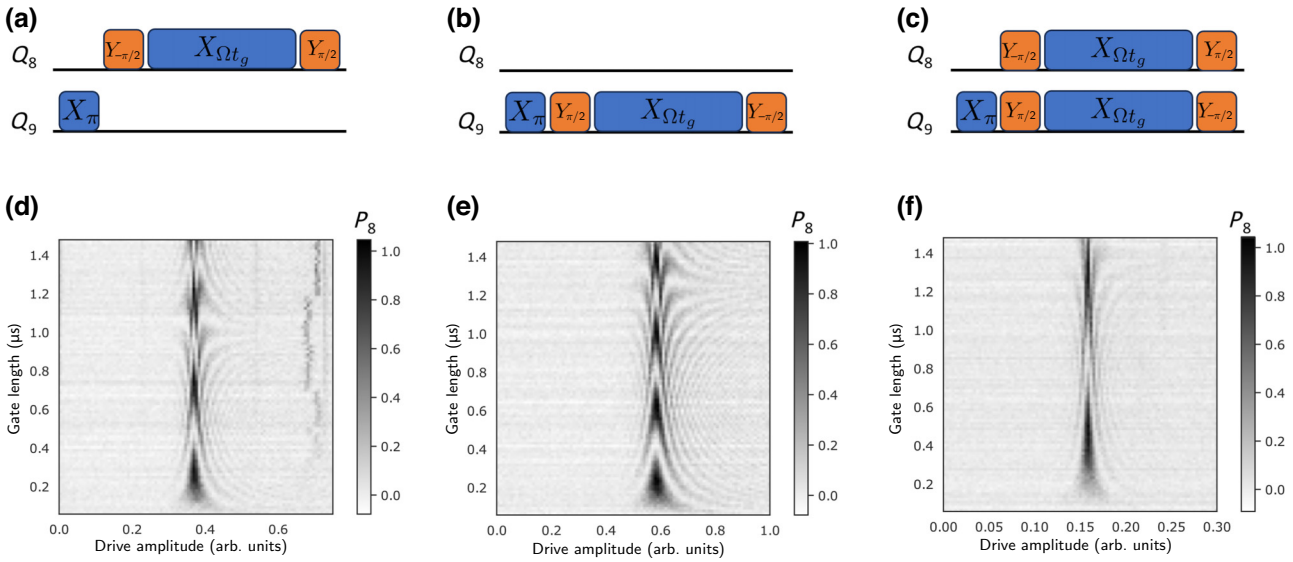

FIG. 1. Pulse sequences for realizing *i*SWAP interaction using on-resonant drives. (a) Lower-frequency qubit Q_8 is driven, (b) higher-frequency qubit Q_9 is driven, and (c) both qubits are driven (FLICFORQ). Coherent oscillations are observed when $\Omega = \Delta$. The excitation probability of Q_8, denoted P_8, for the three pulse sequences is shown in (d)–(f). Note that the oscillation rate for one-qubit driving is nearly twice the rate of FLICFORQ. For two-qubit driving, the Rabi amplitudes need not be the same. In (d) we observe two-level-system (TLS) interactions characterized by peaks randomly moving in time. Using on-resonant drives (spin locking) to study TLS dynamics has been investigated in Refs. [16,17].

effective Hamiltonian becomes

$$\begin{aligned} Y_{\pm\pi/2} H_D Y_{\mp\pi/2} &= \mp\frac{\Omega}{2}(ZI - \mu XX) - \frac{\Delta}{2}IZ \\ &= \mp\frac{\Omega}{2}ZI - \frac{\Delta}{2}IZ \pm \frac{\mu\Omega}{4}(XX + YY) \\ &\quad \pm \frac{\mu\Omega}{4}(XX - YY). \end{aligned}$$

Depending on the sign of Δ, one can choose the appropriate single-qubit rotations $Y_{\pm\pi/2}$ to drive either *i*SWAP ($XX + YY$) or *b*SWAP ($XX - YY$) gates. In this section we focus on the *i*SWAP gate. In Sec. IV we show that the *i*SWAP and *b*SWAP gates can also be realized from off-resonant drives. The final unitary needs frame tracking to become an *i*SWAP gate. Using Eqs. (1) and (2), we can parameterize the unitary as

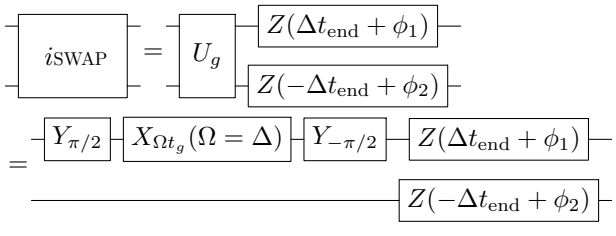

(3)

where $U_g = Y_{\pi/2} X_{\Omega t_g} Y_{-\pi/2}$ and $X_{\Omega t_g} = e^{-iH_D t_g}$. Here ϕ_1 and ϕ_2 are time-independent phases; their calibration sequences are presented in Appendix C 1. In order to use this *i*SWAP gate in a quantum circuit, we construct a pass manager in Qiskit that does the following: (1) schedule the quantum circuit, locate each *i*SWAP gate, and insert two virtual Z rotations (frame changes) at the end of *i*SWAP gate according to Eq. (3); (2) move all the frame changes to the end of the circuit, move frame changes across *i*SWAP gates according to Eq. (2). Note that Z rotations remain virtual throughout the circuit and contribute no extra time, thus preserving the validity of the original schedule. A similar approach has recently been demonstrated to track *i*SWAP frames in a fluxonium processor [28]. We apply the aforementioned pass manager to IRB circuits to benchmark native *i*SWAP gates constructed from on-resonant drives. The IRB data are shown in Fig. 2. The native *i*SWAP gate is realized by resonantly driving the lower-frequency qubit Q_8. We measure an error per gate (EPG) of 0.00648(21) for the native *i*SWAP gate, an EPG of 0.01224(27) for the compiled *i*SWAP gate using two CZ gates, and an EPG of 0.00666(24) for the CZ gate. For the IRB experiments, we use 64-ns single-qubit gates and a 270-ns on-resonant drive so the total *i*SWAP gate time is 398 ns. The CZ gate is an echoed CR gate with target rotary [3,11,29] and has a gate time of 512 ns. The pulse sequence for the CZ gate is shown in Appendix B. The single-qubit gates are Gaussian pulses and 4σ long. Both the on-resonant and CR drives are flat-topped Gaussian pulses where the rise and fall are 2σ long with $\sigma \approx 14.22$ ns. All qubit parameters for the experiments including coherence times are summarized in Table I; device properties of the quantum processor can be found in the

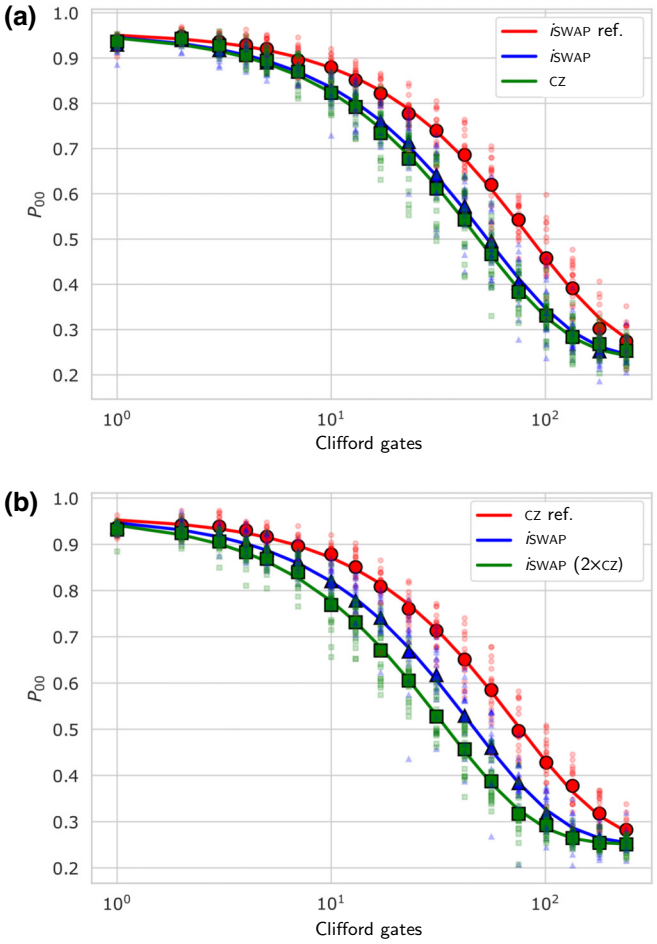

FIG. 2. Interleaved RB data. Panel (a) uses the native *i*SWAP gate in the reference RB, and interleaves the native *i*SWAP and CZ gates based on CR. Panel (b) uses the CZ gate in the reference RB, and interleaves the native *i*SWAP and compiled *i*SWAP gates using two CZ gates. The native *i*SWAP gate is realized by driving Q_8 resonantly, and the CZ gate is realized by driving Q_9 at the frequency of Q_8 (CR). Here P_{00} represents the probability of returning to the $|00\rangle$ state. Large plot markers represent the average over 20 RB realizations (small markers); solid lines are exponential fits to the average. The measured EPG for the native *i*SWAP gate is 0.00648(21).

supplemental materials of Ref. [1]. We also note a recent work implementing the *i*SWAP gate using simultaneous CR interactions [30].

A. Direct SWAP gate

We can augment the direct *i*SWAP gate constructed using on-resonant drives into a direct SWAP gate by applying a CR pulse on the idling qubit. In addition to $XX + YY$, the SWAP gate needs ZZ. The CR pulse on the idling qubit generates XZ, which gets transformed into ZZ by the single-qubit $Y_{\pm\pi/2}$ rotations. The frame tracking for the

TABLE I. Summary of the qubit parameters used in this work. The 1Q (one-qubit) RB numbers are error per Clifford measured from the gate set consisting of $X_{\pm\pi/2}$, $Y_{\pm\pi/2}$, $Z_{\pm\pi/2}$, and $Z_{0,\pi}$; all Z rotations are virtual frame changes [20]. On the quantum processor, $Q_{8,9}$ are connected and $Q_{8,12}$ are connected.

Parameters	Q_8	Q_9	Q_{12}
f_{01} (GHz)	4.726	4.780	4.850
α (MHz)	−333	−332	−332
T_1 (μs)	277(9)	231(5)	184(4)
$T_{2\text{echo}}$ (μs)	53(4)	219(14)	334(26)
1Q RB	$2.24(53) \times 10^{-4}$	$1.50(36) \times 10^{-4}$	$1.69(40) \times 10^{-4}$

SWAP gate is identical to the *i*SWAP gate:

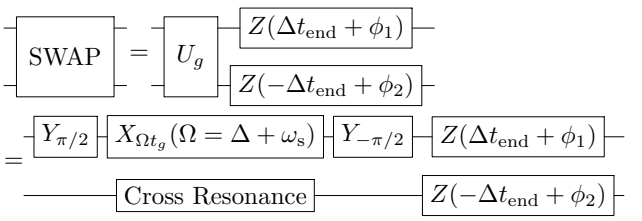

(4)

The phases $\phi_{1,2}$ are calibrated differently from the *i*SWAP gate; see Appendix C 2 for details. The calibration routine for the direct SWAP gate is the following. First the amplitude of the CR drive is calibrated to generate an XZ rotation of $\pi/2$ for the same gate time as the direct *i*SWAP gate. Then the Rabi amplitude Ω of the on-resonant drive is calibrated; note that the resonance condition is $\Omega = \Delta + \omega_s$, where ω_s is the Stark shift on the idling qubit generated by the CR pulse. Finally, $\phi_{1,2}$ are calibrated and the frame tracking is applied in software via the pass manager in Qiskit. We show benchmarking results for the direct SWAP gate in Fig. 3. The direct SWAP gate uses the same set of qubits ($Q_{8,9}$), and has the same length as the *i*SWAP gate (398 ns). We realize the SWAP gate by driving resonantly on Q_8 and simultaneously applying CR on Q_9 at Q_8's frequency. The measured EPGs are 0.00821(23) for the native SWAP gate and 0.02039(38) for the compiled SWAP gate using three CZ gates.

IV. OFF-RESONANT (STARK) *i*SWAP AND *b*SWAP GATES

A recent work shows that the *i*SWAP gate can be realized by driving both qubits off resonantly [31]. The idea is to drive the lower-frequency qubit from below and the higher-frequency qubit from above; the *i*SWAP gate is realized when the sum of the Stark shifts becomes equal to the detuning of the qubits. By adding a third tone to one of the qubits, it is possible to realize programmable Heisenberg interactions [31]. Here we generate a native *i*SWAP gate using one off-resonant drive with the resonance condition $\omega_s = -\Delta$. To see how the gate works, we start from

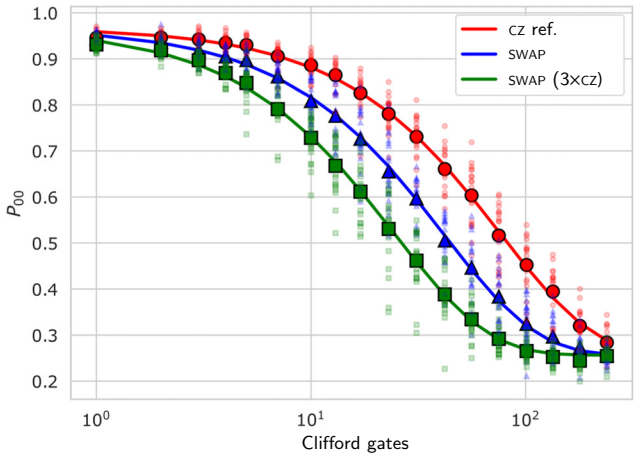

FIG. 3. Interleaved RB data for the native SWAP gate realized by simultaneously driving Q_8 on resonant and Q_9 off resonant. The reference RB uses the CZ gate based on CR; the interleaved gates are the native SWAP and compiled SWAP gates using three CZ gates. The measured EPG for the native SWAP gate is 0.00821(23).

the drive Hamiltonian

$$H_D = \frac{\Omega}{2}(XI + \mu ZX) + \frac{\lambda}{2}ZI - \frac{\Delta - \lambda}{2}IZ,$$

where $\lambda = \omega_1 - \omega_D$ is the detuning of the drive and Δ is the frequency difference between the two qubits. We can rewrite the drive Hamiltonian as

$$H_D = \frac{\Omega'}{2}Z'I - \frac{\Delta - \lambda}{2}IZ + \frac{\mu\Omega}{2}ZX,$$

where $\Omega' = \sqrt{\Omega^2 + \lambda^2}$ and $Z' = (\Omega X + \lambda Z)/\Omega'$. Since the axes Z' and Z are not the same, the Stark *i*SWAP gate will have non-Markovian gate errors that must be corrected by applying DRAG [12,31]. Intuitively, DRAG correction works by rotating Z' into Z; its function is similar to the $Y_{\pm\pi/2}$ gates in an on-resonant *i*SWAP gate. The final Hamiltonian for the Stark *i*SWAP gate is given by

$$H_D = \frac{\mathrm{sign}(\lambda)\Omega'}{2}ZI - \frac{\Delta - \lambda}{2}IZ - \frac{\mu\Omega\lambda}{2\Omega'}XX + \frac{\mu\Omega^2}{2\Omega'}ZX. \tag{5}$$

In order to drive the *i*SWAP gate, we need the coefficients of ZI to match those of IZ. This leads to the resonance condition $\omega_s = -\Delta$, where ω_s is the Stark shift defined as $\omega_s = \mathrm{sign}(\lambda)\sqrt{\Omega^2 + \lambda^2} - \lambda$. The frame tracking for the Stark *i*SWAP gate,

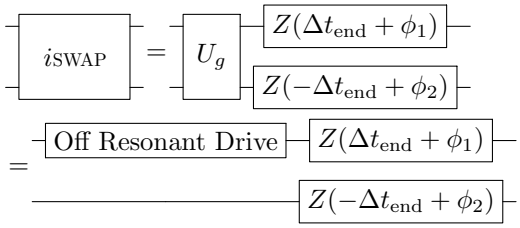

is exactly the same as the native *i*SWAP gate realized with on-resonant drive. The only difference being that the single-qubit rotations $Y_{\pm\pi/2}$ are no longer needed. We show IRB results in Fig. 4(a). The Stark *i*SWAP gate is realized by driving Q_8 60 MHz below its resonant frequency. The measured EPG for the Stark *i*SWAP gate is 0.00409(27), and the gate time is 192 ns. We remark that we can also augment the Stark *i*SWAP gate into a native SWAP gate by driving the idling qubit off resonantly at the same frequency, and we can adjust the phase differences between the two drives to get ZZ in addition to $XX + YY$ using the mechanism described in Refs. [6,7,31].

Next we show how to realize a native *b*SWAP gate by driving one qubit off resonantly. The *b*SWAP gate has the interaction $XX - YY$ and is unitarily equivalent to the *i*SWAP gate up to single-qubit rotations [32]. From the drive Hamiltonian in Eq. (5), we can resonantly excite $XX - YY$ provided that the coefficients of ZI are negative to those of IZ; this leads to the resonance condition $\omega_1 + \omega_2 + \omega_s = 2\omega_D$. Here $\omega_{1,2,s,D}$ are the qubit one frequency, qubit two frequency, Stark shift, and drive frequency respectively. Phases can be moved across the *b*SWAP gate as

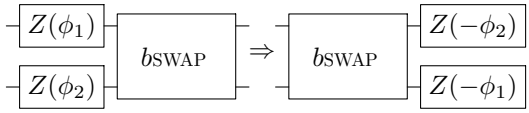

Combined with the frame tracking

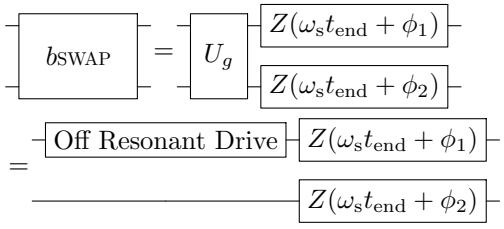

we can benchmark the *b*SWAP gate in Qiskit just the same as the *i*SWAP gate. However *b*SWAP frame tracking uses ω_s instead of the detuning between qubits Δ. The phases for the *b*SWAP gate are calibrated according to Appendix C 3. We realize the native *b*SWAP gate for two qubits ($Q_{8,12}$) separated by 124 MHz by driving the higher-frequency qubit 44 MHz below its resonant frequency. The *b*SWAP gate has

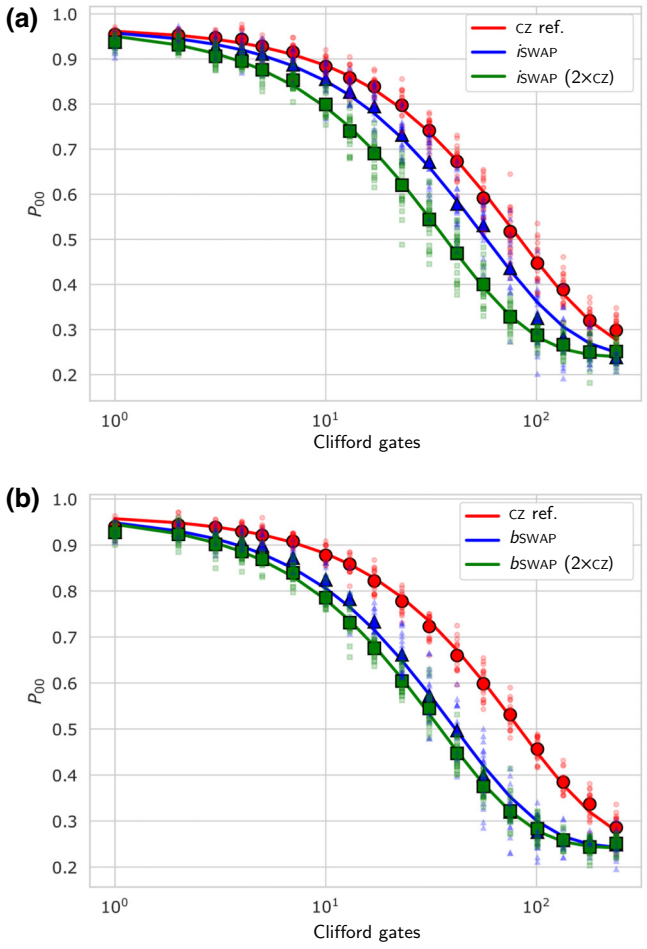

FIG. 4. Interleaved RB data for (a) Stark *i*SWAP and (b) *b*SWAP gates. The IRB experiments used 20 realizations. The measured EPG for the Stark *i*SWAP gate is 0.00409(27) and for the Stark *b*SWAP gate is 0.00936(39).

a gate time of 462 ns. In Fig. 4(b) we show the IRB result of the *b*SWAP gate. We measure an EPG of 0.00936(39) for the native *b*SWAP gate and 0.01265(46) for the compiled *b*SWAP gate using two CZ gates.

We expect the *b*SWAP gate fidelity to decrease for qubit pairs with small detunings, since the driving frequency will become too close to the qubit frequency. For large detuning pairs, we expect the *i*SWAP gate fidelity to decrease because of the large Rabi drive and Stark shift required. Thus, having both *b*SWAP and *i*SWAP gates available in a multiqubit processor can be beneficial as they can complement each other. Finally, we expect the last term in Eq. (5) to have a small contribution to the gate error when resonance conditions are met.

V. NON-CLIFFORD GATES

A. $\sqrt{i\text{SWAP}}$ gate

We present two realizations of the $\sqrt{i\text{SWAP}}$ gate using on-resonant and off-resonant driving on one qubit. There are two crucial differences between realizing the *i*SWAP gate and the $\sqrt{i\text{SWAP}}$ gate. Since we can no longer move frame changes across the gate like we did for the *i*SWAP gate, frame tracking must be done before and after the gate. Secondly, we need three instead of two time-independent phases to tune up the $\sqrt{i\text{SWAP}}$ gate. The frame tracking is done according to

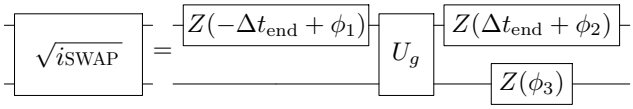

where U_g is realized by driving the first qubit either on resonant sandwiched by single-qubit gates or off resonant. We need to calibrate three instead of four time-independent phases because of the property $[XX + YY, ZI + IZ] = 0$; we can always move the same phases on both qubits across the $\sqrt{i\text{SWAP}}$ gate. The procedure for calibrating $\phi_{1,2,3}$ is outlined in Appendix C 4.

For the direct $\sqrt{i\text{SWAP}}$ gate using on-resonant drives, we have modified the pass manager to first combine the two single-qubit gates $Y_{\pm\pi/2}$ with other single-qubit gates between two $\sqrt{i\text{SWAP}}$ gates, and then apply the frame tracking. This allows us to further shorten the gate time. For the direct $\sqrt{i\text{SWAP}}$ gate using off-resonant drives, we reduce the length of the Stark *i*SWAP gate to approximately half. The total gate time for the on-resonant $\sqrt{i\text{SWAP}}$ gate is 149 ns and for the off-resonant $\sqrt{i\text{SWAP}}$ gate is 117 ns. We use IRB to benchmark the *i*SWAP gate made out of two direct $\sqrt{i\text{SWAP}}$ gates; the results are shown in Fig. 5. Note that physical Z rotations no longer preserve the original schedule, and thus the act of frame tracking itself changes the time-dependent frames in the circuit. Therefore we provision extra general single-qubit gates (U) prior to scheduling. All frames as well as any inherent single-qubit gates of the circuit will be absorbed into this U gate, which makes the schedule deterministic. All U gates are constructed using three pulses [21].

We observe an improved EPG for $\sqrt{i\text{SWAP}}$ gates over *i*SWAP gates for both on-resonant and off-resonant driving. While the $\sqrt{i\text{SWAP}}$ gate has lower error rates and is more efficient than the *i*SWAP gate in constructing general SU(4) operations, its inability to work with virtual Z rotations may undermine the aforementioned advantages in processors where single-qubit gates are less ideal. The technique used to realize the Stark $\sqrt{i\text{SWAP}}$ gate can be applied to realize the $\sqrt{b\text{SWAP}}$ gate as well. We note that recent works have also realized $\sqrt{i\text{SWAP}}$ gates in fluxonium processors [33,34].

B. *B* gate

The B gate is the most efficient two-qubit gate in terms of compiling to SU(4) unitaries; any SU(4) can be compiled using single-qubit gates and two B gates [8]. The

unitary of the B gate is given by $e^{i\pi(2XX+YY)/4}$. Because of the asymmetry between the two Ising interactions in the B gate unitary, it is not clear if there exits a native implementation of the B gate. Here we realize the B gate natively by combining $i\text{SWAP}^{3/4}$ and $b\text{SWAP}^{1/4}$ gates constructed using on-resonant drives described in Sec. III. Note that the bSWAP interaction can be generated by changing the single-qubit rotations $Y_{\pm\pi/2}$ or the on-resonant drive from $+X$ to $-X$ in the iSWAP gate; however, the frame tracking is reversed. The overall frame tracking for the B gate is given by

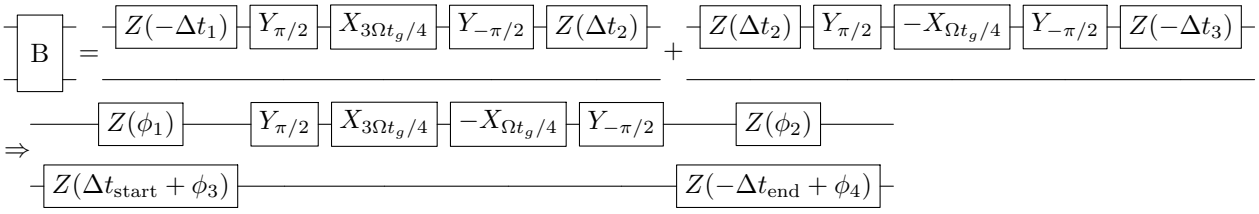

(6)

where we have used the properties $[XX + YY, ZI + IZ] = 0$ and $[XX - YY, ZI - IZ] = 0$ to move the phases in between the $+X$ and $-X$ drives to the front and back of the gate. Interesting, frame tracking for the B gate is applied only on the idle qubit. Similar to the $\sqrt{i\text{SWAP}}$ gate, we can go one step further and absorb the single-qubit gates $Y_{\pm\pi/2}$ into single-qubit unitaries in between B gates. Thus, the native implementation of the B gate consists of just two on-resonant drives $+X$ and $-X$, with the $+X$ drive approximately 3 times as long as the $-X$ drive. There are four time-independent phases $\phi_{1,2,3,4}$ that need to be calibrated for the B gate; their calibration sequences are given in Appendix C 5. We construct an iSWAP gate using two B gates and benchmark using IRB. The results are shown in Fig. 6. The native B gate is 302 ns long, with the $+X$ and $-X$ drives being 210 ns and 92 ns, respectively. The drives are flat-topped Gaussian pulses where the rise and fall are 2σ long with $\sigma \approx 14.22$ ns. The measured EPG for the B gate is comparable to the iSWAP gate; this is expected since both gates are using the same mechanism and have comparable gate times. Similar to the $\sqrt{i\text{SWAP}}$ gate, whether the efficiency of the B gate outweighs the lack of virtual Z rotations will be an important consideration for multiqubit circuits. Finally, we remark that by combining on-resonant drives of opposite signs and CR, we can generate native two-qubit interactions of the form

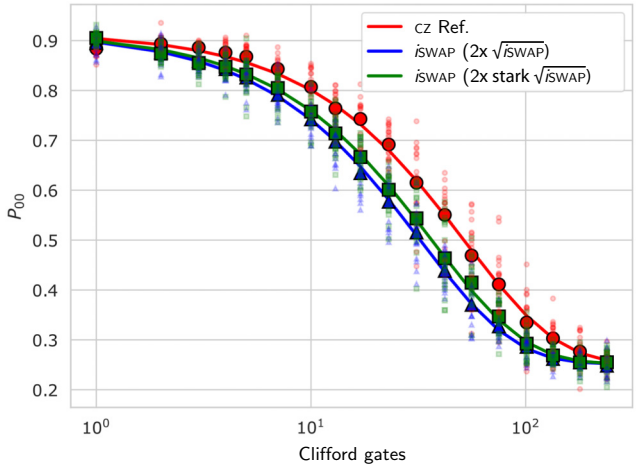

FIG. 5. Interleaved RB data for the $\sqrt{i\text{SWAP}}$ gate. Twenty RB realizations are used. The interleaved element is an iSWAP gate composed of two $\sqrt{i\text{SWAP}}$ gates. The EPG is estimated by dividing the EPG of the iSWAP gate by 2. The EPG for the on-resonant $\sqrt{i\text{SWAP}}$ gate is 0.00427(16), and the EPG for the Stark $\sqrt{i\text{SWAP}}$ gate is 0.00294(15).

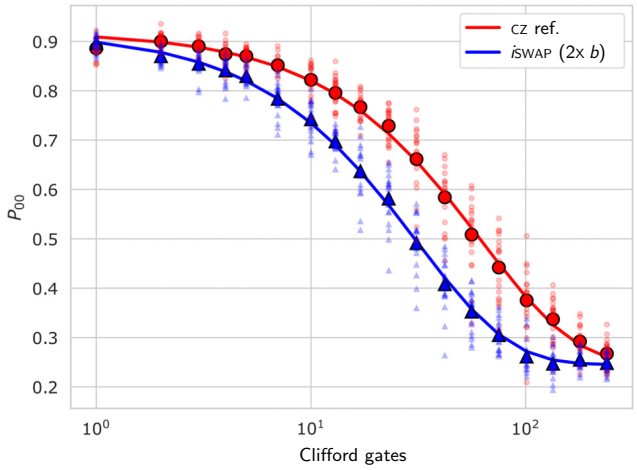

FIG. 6. Interleaved RB data for the B gate. The interleaved element is an iSWAP gate composed of two B gates. The estimated EPG of the B gate is 0.00600(21), obtained by dividing the EPG of the iSWAP gate by 2.

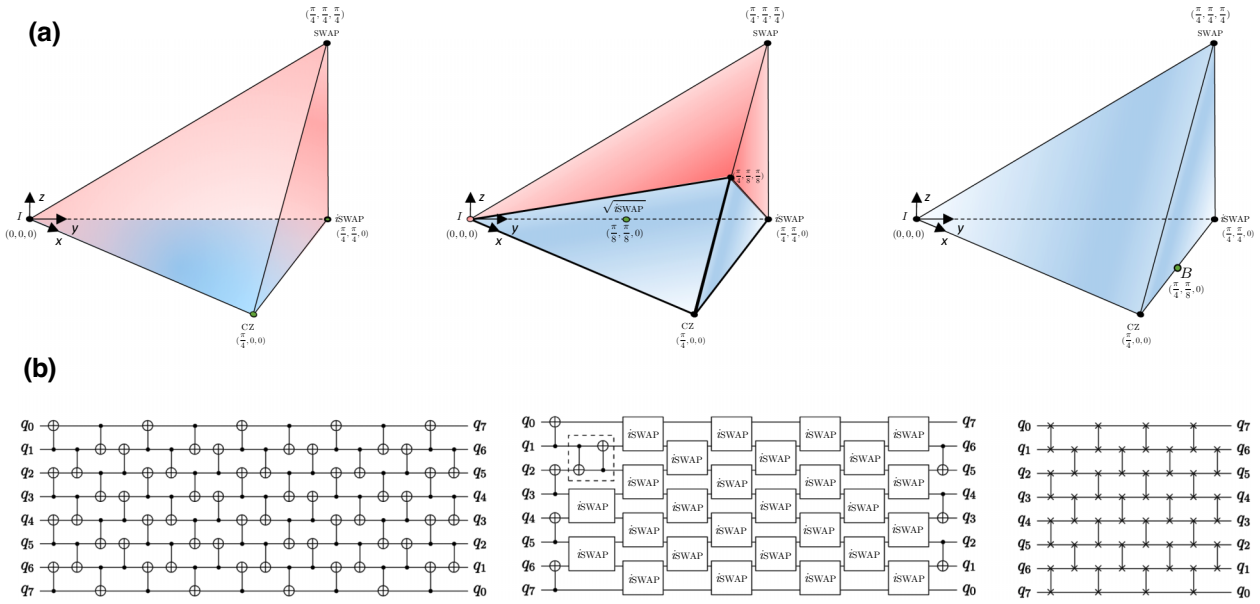

FIG. 7. Building circuits out of more expressive native gates. (a) Regions of the Weyl chamber reachable by two (blue) or three (red) applications of the CZ gate or *i*SWAP gate (left), the $\sqrt{i\text{SWAP}}$ gate (middle), and the *B* gate (right). (b) Circuit compilation for the reversal of an *n*-qubit chain. The circuit requires depth $2n+2$ using only CZ (or CNOT) gates (left). Adding native *i*SWAP gates reduces the depth to $n+2$ (middle), and native SWAP gates require depth *n* (right).

$aXX + bYY + cZZ$ with arbitrary coefficients. The *B* gate is a special case with $c = 0$ and $a = 2b$, and the SWAP gate is another with $a = b = c$. With the appropriate single-qubit gates, our technique can generate arbitrary $SU(4)$ unitaries natively. We recently became aware of the related work by Chen *et al.* [35].

VI. APPLICATION TO CIRCUITS

The gates that we demonstrate in this work can create a richer and more expressive native instruction set on the hardware, which in turn can enable shorter and more efficient quantum circuits [33,36]. In this section we discuss some potential applications of these gates in improving multiqubit circuits.

As a first example, consider random two-qubit unitaries. These appear in quantum benchmarking protocols such as quantum volume, but also routinely during the compilation of circuits. In the latter setting, a compiler performs peephole optimization by collecting a sequence of single- and two-qubit gates, represents it as an instance of a two-qubit unitary, and attempts to resynthesize it with a lower cost. A common representation of the space of all two-qubit unitaries, SU(4), is the Weyl chamber [37]. In this picture, any two-qubit unitary has a unique coordinate, up to local pre- or postrotations. By repeated application of available native gates, one can traverse a path to reach a target unitary. The shorter this path, the higher the fidelity of the compiled circuit. Figure 7(a) shows the region of unitaries reachable using various gates studied in this work. As we move from the CZ gate to the $\sqrt{i\text{SWAP}}$ gate to the *B* gate, we gain a more expressive gate set that is able to reach more of the Weyl chamber with shorter paths.

We can consider other examples such as qubit permutations, an important task in limited-connectivity quantum processors. Figure 7(b) shows possible circuits for the reversal of a chain of qubits on a linear-nearest-neighbor architecture, given different native gates. Using only CZ (or CNOT) gates, this circuit can be accomplished in depth $2n+2$ [38]. However, given access to *i*SWAP gates as well, the same circuit can be realized in depth $n+2$. Finally, native SWAP gates can slightly improve the depth to *n*. While qubit reversals are important, for example, in performing quantum Fourier transforms or more general permutations [39], our construction using native *i*SWAP gates can extend to improve nearly all CNOT circuits on limited-connectivity hardware [40].

VII. CONCLUSION

In this manuscript we have implemented and benchmarked native *i*SWAP, SWAP, *b*SWAP, $\sqrt{i\text{SWAP}}$, and *B* gates in a fixed-frequency, fixed-coupling superconducting processor. A novel software time-dependent frame tracking technique is developed in Qiskit to correctly compile quantum circuits using these native two-qubit gates. We present in Table II the EPGs measured, and in Table III a summary of all the frame tracking used in each native two-qubit gate. We believe that deploying these native gates in large-scale superconducting processors could potentially benefit

TABLE II. Summary of EPGs for all the native two-qubit gates realized in this work. Gates with an asterisk are benchmarked with single-qubit rotations included.

Gate	EPG	Qubits used	Length (ns)
*i*SWAP	0.00648(21)	[8, 9]	398*
SWAP	0.00821(23)	[8, 9]	398*
Stark *i*SWAP	0.00409(27)	[8, 9]	192
Stark *b*SWAP	0.00936(39)	[8, 12]	462
$\sqrt{i\text{SWAP}}$	0.00427(16)	[8, 9]	149
Stark $\sqrt{i\text{SWAP}}$	0.00294(15)	[8, 9]	117
B	0.00600(21)	[8, 9]	302
CZ	0.00666(24)	[8, 9]	512*

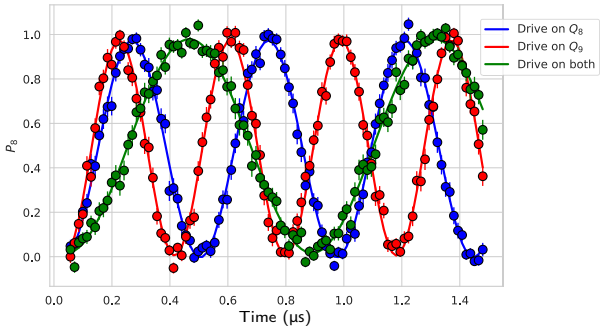

FIG. 8. The Q_8 population as a function of time for the three driving scenarios shown in Fig. 1. The points with one-standard-deviation error bars are experimental data, and the curves are fits.

near-term applications. The techniques developed for realizing these gates can be readily extended to qutrit systems [41]. Another important direction is to investigate the collision bounds for these gates [42–44]; specifically, are they more flexible than CR gates in a fixed-coupling architecture? Preliminary work points to the fact that these gates, like CR, might not work particularly well for very large detuning pairs; more studies are needed to understand why. Lastly, the frame tracking capabilities developed in Qiskit are general and can be readily applied to other architectures employing phase-sensitive two-qubit gates, such as the tunable architecture developed in Refs. [45,46].

ACKNOWLEDGMENTS

The authors would like to thank Oliver Dial, Karthik Siva, Matthias Steffen, Jiri Stehlik, and David Zajac for insightful discussions. This work was partially supported by the U.S. Department of Energy, Office of Science, National Quantum Information Science Research Centers, Co-design Center for Quantum Advantage (C2QA) under Contract No. DE-SC0012704.

APPENDIX A: *i*SWAP OSCILLATIONS

Here we show in Fig. 8 the oscillation dynamics for the on-resonant *i*SWAP drives. We fix the amplitude at the resonance point and sweep the length of the drive. We fit the oscillations to the equation $a\sin^2(2\pi ft + b) + c$, where a, b, f, and c are fitting parameters with f the frequency. From the fits we find a rate of 1.062(2) MHz for driving on Q_8, 1.308(2) MHz for driving on Q_9, and 0.590(2) MHz for driving on both Q_8 and Q_9. Simultaneous driving achieves an *i*SWAP rate that is approximately half of that obtained from individual driving.

APPENDIX B: CZ GATE SEQUENCE

The pulse sequence for the CZ gate based on CR interaction is given by

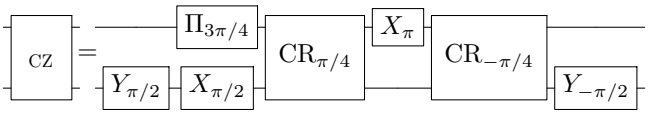

where $\Pi_{3\pi/4} = X_\pi\cos(3\pi/4) + Y_\pi\sin(3\pi/4)$ and $\text{CR}_{\pi/4} = ZX_{\pi/4}$ is the cross-resonance interaction.

APPENDIX C: PHASE CALIBRATIONS

Here we present the pulse sequences used to calibrate the time-independent phases required to realize each two-qubit gate. The first qubit is driven and the second qubit is idle. For *i*SWAP, *b*SWAP, and SWAP gates, there are two phases $\phi_{1,2}$; for the $\sqrt{i\text{SWAP}}$ gate, there are three phases $\phi_{1,2,3}$; and for the *B* gate, there are four phases $\phi_{1,2,3,4}$. All Z rotations in the calibration sequences are implemented as virtual frame changes. All pulse sequences are Ramsey-type experiments that produce a signal in the form $P \propto [1 + \cos(\phi - \phi_i)]/2$, where ϕ is varied. The CNOT gates used in some calibration sequences are based on the CR interaction.

The calibration sequences for *i*SWAP, *b*SWAP, and SWAP gates are similar to single-qubit Ramsey experiments, except the second $\pi/2$ pulse is applied on the other qubit since the gate unitary switches the phases. The calibration sequences for the $\sqrt{i\text{SWAP}}$ and *B* gates use the CNOT gate instead of $\pi/2$ gate. It is a two-qubit version of the Ramsey experiment where we are trying to calibrate the relative phase in a Bell state such as $|00\rangle + e^{i\phi}|11\rangle$.

TABLE III. Summary of native two-qubit gates realized in this work.

Gate	Interaction	Unitary	Resonance condition	Frame tracking
*i*SWAP (on resonant)	$XX+YY$	$\begin{pmatrix}1&0&0&0\\0&0&i&0\\0&i&0&0\\0&0&0&1\end{pmatrix}$	$\Omega=\Delta$	$Z(\pm\Delta t_{\text{end}})$ behind the driven and idle qubits
SWAP	$XX+YY+ZZ$	$\begin{pmatrix}1&0&0&0\\0&0&1&0\\0&1&0&0\\0&0&0&1\end{pmatrix}$	$\Omega=\Delta+\omega_{\text{s}}$	$Z(\pm\Delta t_{\text{end}})$ behind the driven and idle qubits
*i*SWAP (Stark)	$XX+YY$	$\begin{pmatrix}1&0&0&0\\0&0&i&0\\0&i&0&0\\0&0&0&1\end{pmatrix}$	$\omega_{\text{s}}=\Delta$	$Z(\pm\Delta t_{\text{end}})$ behind the driven and idle qubits
*b*SWAP (Stark)	$XX-YY$	$\begin{pmatrix}0&0&0&i\\0&1&0&0\\0&0&1&0\\i&0&0&0\end{pmatrix}$	$\omega_1+\omega_2+\omega_{\text{s}}=2\omega_D$	$Z(\omega_{\text{s}}t_{\text{end}})$ behind the driven and idle qubits
$\sqrt{i\text{SWAP}}$ (on resonant)	$XX+YY$	$\begin{pmatrix}1&0&0&0\\0&1/\sqrt{2}&i/\sqrt{2}&0\\0&i/\sqrt{2}&1/\sqrt{2}&0\\0&0&0&1\end{pmatrix}$	$\Omega=\Delta$	$Z(\pm\Delta t_{\text{end}})$ in front of and behind the driven qubit
$\sqrt{i\text{SWAP}}$ (Stark)	$XX+YY$	$\begin{pmatrix}1&0&0&0\\0&1/\sqrt{2}&i/\sqrt{2}&0\\0&i/\sqrt{2}&1/\sqrt{2}&0\\0&0&0&1\end{pmatrix}$	$\omega_{\text{s}}=\Delta$	$Z(\pm\Delta t_{\text{end}})$ in front of and behind the driven qubit
B gate	$2XX+YY$	$\begin{pmatrix}\cos(\pi/8)&0&0&i\sin(\pi/8)\\0&\sin(\pi/8)&i\cos(\pi/8)&0\\0&i\cos(\pi/8)&i\sin(\pi/8)&0\\i\sin(\pi/8)&0&0&\cos(\pi/8)\end{pmatrix}$	$\Omega=\Delta$	$Z(\mp\Delta t_{\text{end}})$ in front of and behind the idle qubit

1. *i*SWAP phase calibrations

We have

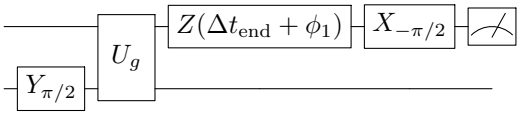

and

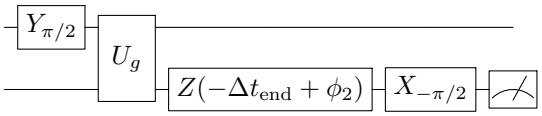

2. SWAP phase calibrations

We have

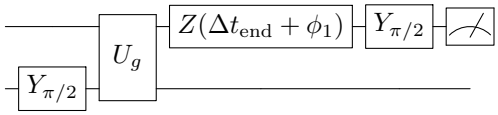

and

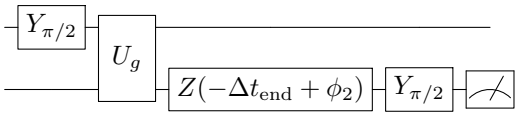

3. *b*SWAP phase calibrations

We have

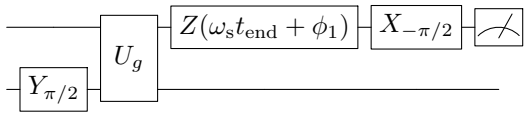

and

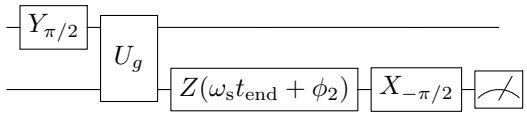

4. $\sqrt{i\text{SWAP}}$ phase calibrations

We have

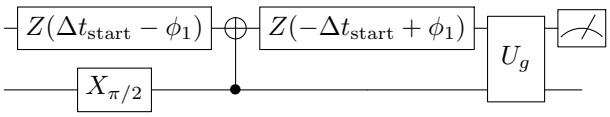

Let $\phi_{t,d} = \phi_2 \pm \phi_3$, $\phi_{t,d}$ be calibrated according to the following sequences:

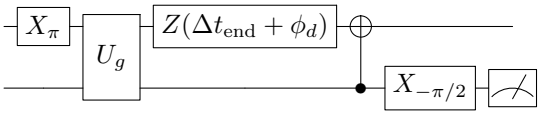

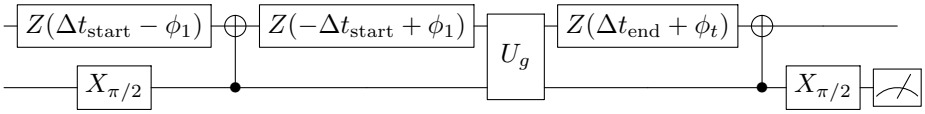

5. *B*-gate phase calibrations

Let $\varphi_{t,d} = \phi_1 \pm \phi_3$, $\varphi_{t,d}$ be calibrated according to the following sequences:

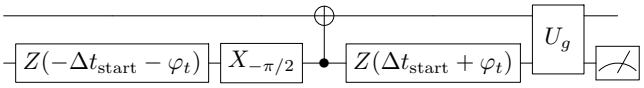

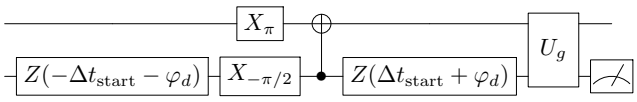

Let $\phi_{t,d} = \phi_2 \pm \phi_4$, $\phi_{t,d}$ be calibrated according to the following sequences

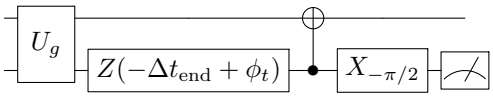

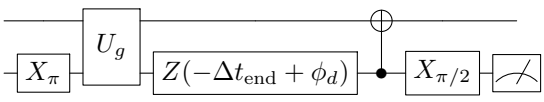

[1] Y. Kim, A. Eddins, S. Anand, K. X. Wei, E. van den Berg, S. Rosenblatt, H. Nayfeh, Y. Wu, M. Zaletel, K. Temme, and A. Kandala, Evidence for the utility of quantum computing before fault tolerance, Nature **618**, 500 (2023).

[2] J. M. Chow, A. D. Córcoles, J. M. Gambetta, C. Rigetti, B. R. Johnson, J. A. Smolin, J. R. Rozen, G. A. Keefe, M. B. Rothwell, M. B. Ketchen, and M. Steffen, Simple all-microwave entangling gate for fixed-frequency superconducting qubits, Phys. Rev. Lett. **107**, 080502 (2011).

[3] S. Sheldon, E. Magesan, J. M. Chow, and J. M. Gambetta, Procedure for systematically tuning up cross-talk in the cross-resonance gate, Phys. Rev. A **93**, 060302 (2016).

[4] A. Patterson, J. Rahamim, T. Tsunoda, P. Spring, S. Jebari, K. Ratter, M. Mergenthaler, G. Tancredi, B. Vlastakis, M. Esposito, and P. Leek, Calibration of a cross-resonance two-qubit gate between directly coupled transmons, Phys. Rev. Appl. **12**, 064013 (2019).

[5] A. Kandala, K. X. Wei, S. Srinivasan, E. Magesan, S. Carnevale, G. A. Keefe, D. Klaus, O. Dial, and D. C. McKay, Demonstration of a high-fidelity CNOT gate for fixed-frequency transmons with engineered *ZZ* suppression, Phys. Rev. Lett. **127**, 130501 (2021).

[6] B. K. Mitchell, R. K. Naik, A. Morvan, A. Hashim, J. M. Kreikebaum, B. Marinelli, W. Lavrijsen, K. Nowrouzi,

D. I. Santiago, and I. Siddiqi, Hardware-efficient microwave-activated tunable coupling between superconducting qubits, Phys. Rev. Lett. **127**, 200502 (2021).

[7] K. X. Wei, E. Magesan, I. Lauer, S. Srinivasan, D. F. Bogorin, S. Carnevale, G. A. Keefe, Y. Kim, D. Klaus, W. Landers, N. Sundaresan, C. Wang, E. J. Zhang, M. Steffen, O. E. Dial, D. C. McKay, and A. Kandala, Hamiltonian engineering with multicolor drives for fast entangling gates and quantum crosstalk cancellation, Phys. Rev. Lett. **129**, 060501 (2022).

[8] J. Zhang, J. Vala, S. Sastry, and K. B. Whaley, Minimum construction of two-qubit quantum operations, Phys. Rev. Lett. **93**, 020502 (2004).

[9] J. M. Chow, J. M. Gambetta, A. W. Cross, S. T. Merkel, C. Rigetti, and M. Steffen, Microwave-activated conditional-phase gate for superconducting qubits, New J. Phys. **15**, 115012 (2013).

[10] F. Arute, *et al.*, GOOGLE AI QUANTUM AND COLLABORATORS, Hartree-Fock on a superconducting qubit quantum computer, Science **369**, 1084 (2020).

[11] P. Jurcevic, *et al.*, Demonstration of quantum volume 64 on a superconducting quantum computing system, Quantum Sci. Technol. **6**, 025020 (2021).

[12] K. X. Wei, E. Pritchett, D. M. Zajac, D. C. McKay, and S. Merkel, Characterizing non-Markovian off-resonant errors in quantum gates, Phys. Rev. Appl. **21**, 024018 (2024).

[13] Qiskit contributors, Qiskit: An open-source framework for quantum computing (2023).

[14] E. Magesan, J. M. Gambetta, and J. Emerson, Scalable and robust randomized benchmarking of quantum processes, Phys. Rev. Lett. **106**, 180504 (2011).

[15] E. Magesan, J. M. Gambetta, B. R. Johnson, C. A. Ryan, J. M. Chow, S. T. Merkel, M. P. da Silva, G. A. Keefe, M. B. Rothwell, T. A. Ohki, M. B. Ketchen, and M. Steffen, Efficient measurement of quantum gate error by interleaved randomized benchmarking, Phys. Rev. Lett. **109**, 080505 (2012).

[16] L. V. Abdurakhimov, I. Mahboob, H. Toida, K. Kakuyanagi, Y. Matsuzaki, and S. Saito, Identification of different types of high-frequency defects in superconducting qubits, PRX Quantum **3**, 040332 (2022).

[17] L. V. Abdurakhimov, I. Mahboob, H. Toida, K. Kakuyanagi, Y. Matsuzaki, and S. Saito, Driven-state relaxation of a coupled qubit-defect system in spin-locking measurements, Phys. Rev. B **102**, 100502 (2020).

[18] M. Malekakhlagh and E. Magesan, Mitigating off-resonant error in the cross-resonance gate, Phys. Rev. A **105**, 012602 (2022).

[19] J. M. Chow, L. DiCarlo, J. M. Gambetta, F. Motzoi, L. Frunzio, S. M. Girvin, and R. J. Schoelkopf, Optimized driving of superconducting artificial atoms for improved single-qubit gates, Phys. Rev. A **82**, 040305(R) (2010).

[20] D. C. McKay, C. J. Wood, S. Sheldon, J. M. Chow, and J. M. Gambetta, Efficient z gates for quantum computing, Phys. Rev. A **96**, 022330 (2017).

[21] J. Chen, D. Ding, C. Huang, and Q. Ye, Compiling arbitrary single-qubit gates via the phase shifts of microwave pulses, Phys. Rev. Res. **5**, L022031 (2023).

[22] D. C. McKay, S. Filipp, A. Mezzacapo, E. Magesan, J. M. Chow, and J. M. Gambetta, Universal gate for fixed-frequency qubits via a tunable bus, Phys. Rev. Appl. **6**, 064007 (2016).

[23] M. O. Tholén, R. Borgani, C. Križan, J. Bylander, and D. B. Haviland, Characterization and benchmarking of a phase-sensitive two-qubit gate using direct digital synthesis, ArXiv:2308.08893.

[24] M. Ganzhorn, G. Salis, D. J. Egger, A. Fuhrer, M. Mergenthaler, C. Müller, P. Müller, S. Paredes, M. Pechal, M. Werninghaus, and S. Filipp, Benchmarking the noise sensitivity of different parametric two-qubit gates in a single superconducting quantum computing platform, Phys. Rev. Res. **2**, 033447 (2020).

[25] D. M. Abrams, N. Didier, B. R. Johnson, M. P. d. Silva, and C. A. Ryan, Implementation of XY entangling gates with a single calibrated pulse, Nat. Electron. **3**, 744 (2020).

[26] C. Rigetti, A. Blais, and M. Devoret, Protocol for universal gates in optimally biased superconducting qubits, Phys. Rev. Lett. **94**, 240502 (2005).

[27] E. Magesan and J. M. Gambetta, Effective Hamiltonian models of the cross-resonance gate, Phys. Rev. A **101**, 052308 (2020).

[28] F. Bao, *et al.*, Fluxonium: An alternative qubit platform for high-fidelity operations, Phys. Rev. Lett. **129**, 010502 (2022).

[29] N. Sundaresan, I. Lauer, E. Pritchett, E. Magesan, P. Jurcevic, and J. M. Gambetta, Reducing unitary and spectator errors in cross resonance with optimized rotary echoes, PRX Quantum **1**, 020318 (2020).

[30] K. Heya and N. Kanazawa, Cross-cross resonance gate, PRX Quantum **2**, 040336 (2021).

[31] L. B. Nguyen, Y. Kim, A. Hashim, N. Goss, B. Marinelli, B. Bhandari, D. Das, R. K. Naik, J. M. Kreikebaum, A. N. Jordan, D. I. Santiago, and I. Siddiqi, Programmable Heisenberg interactions between Floquet qubits, Nat. Phys. **20**, 240 (2024).

[32] S. Poletto, J. M. Gambetta, S. T. Merkel, J. A. Smolin, J. M. Chow, A. D. Córcoles, G. A. Keefe, M. B. Rothwell, J. R. Rozen, D. W. Abraham, C. Rigetti, and M. Steffen, Entanglement of two superconducting qubits in a waveguide cavity via monochromatic two-photon excitation, Phys. Rev. Lett. **109**, 240505 (2012).

[33] C. Huang, T. Wang, F. Wu, D. Ding, Q. Ye, L. Kong, F. Zhang, X. Ni, Z. Song, Y. Shi, H.-H. Zhao, C. Deng, and J. Chen, Quantum instruction set design for performance, Phys. Rev. Lett. **130**, 070601 (2023).

[34] H. Zhang, C. Ding, D. K. Weiss, Z. Huang, Y. Ma, C. Guinn, S. Sussman, S. P. Chitta, D. Chen, A. A. Houck, J. Koch, and D. I. Schuster, Tunable inductive coupler for high-fidelity gates between fluxonium qubits, PRX Quantum **5**, 020326 (2024).

[35] J. Chen, D. Ding, W. Gong, C. Huang, and Q. Ye, in *Proceedings of the 29th ACM International Conference on Architectural Support for Programming Languages and Operating Systems* (Association for Computing Machinery, New York, NY, USA, 2024), Vol. 2, pp. 779–796.

[36] E. C. Peterson, L. S. Bishop, and A. Javadi-Abhari, Optimal synthesis into fixed XX interactions, Quantum **6**, 696 (2022).

[37] J. Zhang, J. Vala, S. Sastry, and K. B. Whaley, Geometric theory of nonlocal two-qubit operations, Phys. Rev. A **67**, 042313 (2003).

[38] S. A. Kutin, D. P. Moulton, and L. M. Smithline, Computation at a distance, ArXiv:quant-ph/0701194.

[39] A. Bapat, A. M. Childs, A. V. Gorshkov, S. King, E. Schoute, and H. Shastri, Quantum routing with fast reversals, Quantum **5**, 533 (2021).

[40] T. G. D. Brugière, M. Baboulin, B. Valiron, S. Martiel, and C. Allouche, Reducing the depth of linear reversible quantum circuits, IEEE Trans. Quantum Eng. **2**, 1 (2021).

[41] N. Goss, A. Morvan, B. Marinelli, B. K. Mitchell, L. B. Nguyen, R. K. Naik, L. Chen, C. Jünger, J. M. Kreikebaum, D. I. Santiago, J. J. Wallman, and I. Siddiqi, High-fidelity qutrit entangling gates for superconducting circuits, Nat. Commun. **13**, 7481 (2022).

[42] J. B. Hertzberg, E. J. Zhang, S. Rosenblatt, E. Magesan, J. A. Smolin, J.-B. Yau, V. P. Adiga, M. Sandberg, M. Brink, J. M. Chow, and J. S. Orcutt, Laser-annealing Josephson junctions for yielding scaled-up superconducting quantum processors, npj Quantum Inf. **7**, 129 (2021).

[43] E. J. Zhang, *et al.*, High-performance superconducting quantum processors via laser annealing of transmon qubits, Sci. Adv. **8**, eabi6690 (2022).

[44] A. Morvan, L. Chen, J. M. Larson, D. I. Santiago, and I. Siddiqi, Optimizing frequency allocation for fixed-frequency superconducting quantum processors, Phys. Rev. Res. **4**, 023079 (2022).

[45] J. Stehlik, D. M. Zajac, D. L. Underwood, T. Phung, J. Blair, S. Carnevale, D. Klaus, G. A. Keefe, A. Carniol, M. Kumph, M. Steffen, and O. E. Dial, Tunable coupling architecture for fixed-frequency transmon superconducting qubits, Phys. Rev. Lett. **127**, 080505 (2021).

[46] D. M. Zajac, J. Stehlik, D. L. Underwood, T. Phung, J. Blair, S. Carnevale, D. Klaus, G. A. Keefe, A. Carniol, M. Kumph, M. Steffen, and O. E. Dial, Spectator errors in tunable coupling architectures, ArXiv:2108.11221 (2021).